

Porous Layered F–N-Doped Carbon Nanofibers for Capacity Enhancement in Flexible Zinc-Ion Batteries Cathodes

Fathiyya Dzikra Azura, Rachendra Akmalia, Yuyun Irmawati, and Afriyanti Sumboja*

Interest in high-capacity flexible zinc-ion batteries has grown due to the demand for wearable electronics. Although porous architecture can enable high-capacity zinc-ion cathodes, they often suffer from poor mechanical properties. Layered structures of porous self-supported cathodes are engineered to address this issue through sequential electrospinning. It features carbon nanofibers layered with manganese oxide nanoparticles embedded in F–N-doped carbon layer, producing a porous yet mechanically robust self-supported $\text{Mn}_x\text{O}_y@\text{PCNF}$ cathode. High surface area ($204 \text{ m}^2 \text{ g}^{-1}$) coupled with improved conductivity and surface wettability through F–N dual doping enhances charge transport

into active Mn_xO_y storage sites and boosts battery capacity. Consequently, in coin cell configuration, $\text{Mn}_x\text{O}_y@\text{PCNF}$ cathode produces high specific capacity of 284 mAh g^{-1} at 0.3 A g^{-1} , outperforming some reported zinc-ion batteries with manganese oxide-based cathodes. With high tensile strength and favorable elastic modulus, $\text{Mn}_x\text{O}_y@\text{PCNF}$ cathode is also successfully implemented in flexible pouch cells with quasisolid gel electrolyte, achieving an average capacity of 130 mAh g^{-1} at 80 mA g^{-1} under various bending angles of 0° – 90° for over 130 charge–discharge cycles. This work offers a promising path to advance energy storage technology in flexible batteries.

1. Introduction

The demand for flexible zinc-ion batteries has risen due to the increased interest in wearable devices.^[1,2] To address the current trend in wearable devices, researchers are focusing on making flexible electrode material, and one of the advancements is in the form of self-supporting electrodes.^[3,4] Self-supporting electrodes are categorized by their ability to hold themselves without using a binder and current collector, and they can both serve as an active material and current collector.^[5] These features mitigate the risk of active material detachment from the current collector, which is often observed in conventional slurry-based cathodes, and thus are suitable for flexible zinc-ion batteries.^[6]

In flexible zinc-ion batteries, self-supported cathodes can be fabricated using N-doped carbon as the host matrix.^[7,8] Besides providing mechanical support, employing N-doped carbon can

enhance the conductivity of low-conductivity zinc-ion cathode materials (e.g., manganese oxides).^[9] Nitrogen atoms can substitute carbon atoms within the carbon lattice, introducing additional electrons into the delocalized π -system and thereby enhancing electrical conductivity.^[10] Despite that, the reported N-doped carbon-based electrodes are generally hydrophobic, leading to low wettability of cathode materials.^[11,12] This may result in poor electrolyte–cathode interface, reduced ion transport, poor utilization of cathode storage sites, and low specific capacity.^[13,14]

Compared to N-doped carbon,^[15,16] additional F-doping has been reported to enhance the surface wettability of carbon-based supercapacitors and oxygen electrocatalysts, owing to its high electronegativity that facilitates the formation of hydrogen bonds with water molecules.^[17,18] High electronegativity of the F atom also further enhances the conductivity of carbon, facilitating better electron transfer.^[19] Combining F and N doping in the carbon anode of potassium-ion battery reduced irreversible K^+ ion adsorption and enhanced the capacity.^[20] Additional F dopant in the N-doped graphene anode of lithium-ion battery increases graphene layer spacing, resulting in higher capacity than single N doping.^[21] Employing dual F–N doping in carbon for zinc-ion batteries, a strategy not yet reported, is expected to improve the conductivity and surface wettability of the zinc-ion cathode materials (e.g., manganese oxides). The improved conductivity from dual F–N doping may facilitate faster charge transfer,^[19] thereby enhancing the redox kinetics of inherently low-conductivity manganese oxides.^[22] Simultaneously, enhanced surface wettability promotes better electrolyte penetration into the active cathode material, enabling more accessible storage sites and increasing the specific capacity of the zinc-ion batteries.^[14]

F. Dzikra Azura, R. Akmalia, A. Sumboja
Materials Science and Engineering Research Group
Faculty of Mechanical and Aerospace Engineering
Institut Teknologi Bandung
Jl. Ganesa 10, Bandung 40132, Indonesia
E-mail: sumboja@itb.ac.id

Y. Irmawati
Doctoral Program of Nanosciences and Nanotechnology
Graduate School
Institut Teknologi Bandung
Jl. Ganesa 10, Bandung 40132, Indonesia

Y. Irmawati
Research Center for Nanotechnology Systems
National Research and Innovation Agency (BRIN),
Tangerang Selatan 15314, Indonesia

 Supporting information for this article is available on the WWW under <https://doi.org/10.1002/batt.202500235>

Electrospinning can be employed to obtain self-supported carbon cathodes doped with F and N.^[23] By simply adding a fluorine precursor, F-doping can be achieved within the N-doped carbon nanofibers. Many fluorine precursors, such as ammonium fluoride, polyvinylidene fluoride (PVDF), and polytetrafluoroethylene (PTFE), can be used in electrospinning.^[24,25] Among them, PTFE possesses double advantages, i.e., source F-doping and pore former during carbonization, producing porous F-doped carbon nanofibers.^[26] This porous structure enhances surface area, leading to more exposed storage sites and increasing ion diffusivity.^[27] However, by increasing its surface area, porous carbon nanofibers will be compromised mechanically.^[28] To solve this problem, a composite design can be implemented as a layered structure by introducing an additional layer that can provide mechanical support.

This work successfully fabricated a porous yet mechanically robust layered self-supported cathode for flexible zinc-ion batteries via sequential electrospinning. The as-spun sample comprises a PVA/PTFE/Mn(Ac)₂ layer on a PAN-based nanofiber layer. After carbonization, it transformed into a layered structure with manganese oxide nanoparticles embedded within a porous

F–N-doped carbon layer that is derived from PVA/PTFE/Mn(Ac)₂, supported by a PAN-derived carbon nanofiber layer ($\text{Mn}_x\text{O}_y@\text{PCNF}$). This layered structure enhances mechanical properties, while dual F–N doping boosts electrochemical performance by improving conductivity and enhancing cathode wettability. Combined with a high surface area of porous structure (204 m² g⁻¹), these features facilitate charge transport into the active Mn_xO_y sites, boosting zinc-ion storage capacity. In coin cell configuration, $\text{Mn}_x\text{O}_y@\text{PCNF}$ cathode yields a high capacity of 284 mAh g⁻¹ at 0.3 A g⁻¹. Employed in flexible quasisolid-state pouch-cell configuration, $\text{Mn}_x\text{O}_y@\text{PCNF}$ cathode also exhibits high and stable performance, demonstrating the viability of the application of $\text{Mn}_x\text{O}_y@\text{PCNF}$ in wearable devices.

2. Results and Discussion

A layered and porous $\text{Mn}_x\text{O}_y@\text{PCNF}$ self-supported cathode was fabricated via sequential electrospinning, as depicted in Figure 1a. PAN solution was first electrospun as the support layer, followed by electrospinning PVA/PTFE/Mn(Ac)₂ solution before

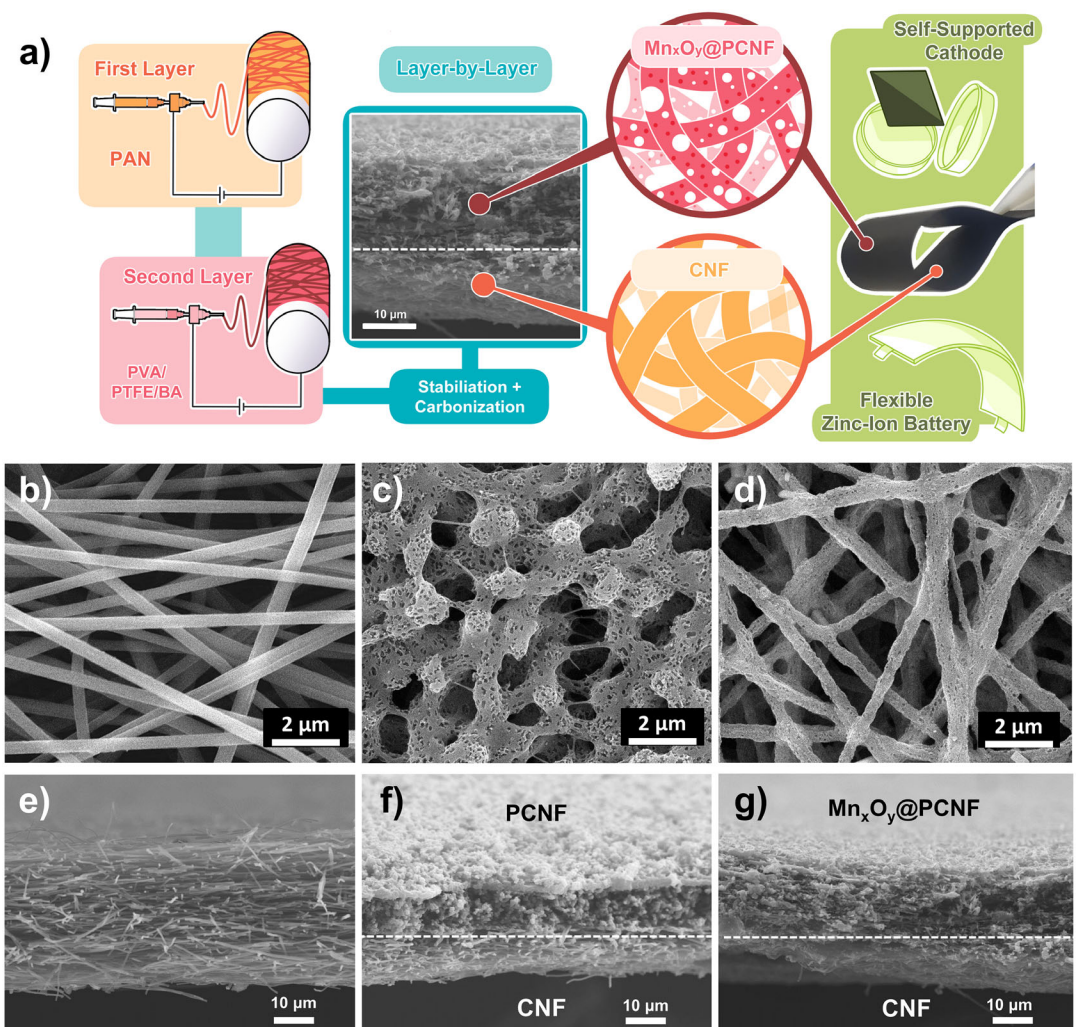


Figure 1. a) Schematic fabrication of $\text{Mn}_x\text{O}_y@\text{PCNF}$ with the inset showing the layered structure of $\text{Mn}_x\text{O}_y@\text{PCNF}$. Surface and cross-sectional SEM images of b,e) CNF, c,f) PCNF, and d,g) $\text{Mn}_x\text{O}_y@\text{PCNF}$, with dotted lines in (f–g) distinguishing the porous and support layers.

being subjected to stabilization and carbonization. During stabilization, the PAN backbone in the support layer undergoes cyclization, initiating crosslinking that enhances the thermal stability of the nanofiber mat.^[29] Without a PAN-support layer, the stabilized single layer of PVA/PTFE/Mn(Ac)₂ mat was too brittle and could not create an integrated free-standing structure (Figure S1, Supporting Information). For comparison, a single PAN layer sample and a layered sample of PAN and PVA/PTFE layers (i.e., without Mn(Ac)₂) were also fabricated and labeled CNF and PCNF, respectively.

Scanning electron microscopy (SEM) images were used to analyze the morphological features of CNF, PCNF, and Mn_xO_y@PCNF samples. Surface morphology of CNF (Figure 1b) shows bulk fiber structures with smooth surfaces, while PCNF (Figure 1c) exhibits globular fibers with porous surfaces. This porous structure is formed by the degradation of PTFE during carbonization,^[26] serving as a sacrificial pore former (Figure S2, Supporting Information). Employing a similar two-layer configuration as PCNF, Mn_xO_y@PCNF also shows porous structures (Figure 1d). However, unlike PCNF, Mn_xO_y@PCNF can sustain linear fiber structures. This is related to the presence of Mn(Ac)₂, which increases the spinning solution's conductivity, enhancing electrostatic forces and stabilizing the electrospinning process. This stabilization ensures a more consistent jet discharge, resulting in fibers with a uniform diameter instead of globular structures.^[30] Compared to globular structures, linear porous nanofibers can create seamless conductive networks, promoting fast charge transfer.^[31]

The cross-sectional SEM of CNF, PCNF, and Mn_xO_y@PCNF samples was observed to analyze the layered structures. Figure 1e shows a cross-sectional SEM image of CNF with a 29.2 μm thickness of a single layer of carbon nanofiber structure. Differently, the layered samples of PCNF and Mn_xO_y@PCNF (Figure 1f-g) exhibit a well-defined two-layer structure with a good interface, featuring an upper porous carbon layer derived from PVA/PTFE-based nanofiber (dark gray) and the bottom carbon nanofiber layer derived from PAN nanofiber (light gray). Both PCNF and

Mn_xO_y@PCNF have PAN-derived carbon nanofiber layers with a similar thickness of around 10.6 μm. However, the upper porous layer in PCNF (11.3 μm) is thinner than that in Mn_xO_y@PCNF (14.4 μm), likely due to greater shrinkage during carbonization driven by increased stress from the globular structure of PCNF.^[32]

N₂ adsorption/desorption analysis was then conducted to quantify surface area of CNF, PCNF, and Mn_xO_y@PCNF. As expected, consistent with the previous study of PAN-derived carbon nanofiber,^[33] CNF has the lowest surface area of 9 m² g⁻¹. With porous structures, there is a significant increase in the surface area of PCNF (369 m² g⁻¹) and Mn_xO_y@PCNF (204 m² g⁻¹). A lower surface area of Mn_xO_y@PCNF than PCNF may relate to the blockage of pores due to the incorporation of metal nanoparticles, as also shown in previous studies.^[34,35] However, Mn_xO_y@PCNF still has a higher surface area compared to reported electrospun carbon nanofiber-based electrodes, ranging from 108 to 165 m² g⁻¹,^[36–38] leading to abundant storage sites and improving the battery capacity.^[39]

Energy-dispersive spectroscopy (EDS) mapping was then performed to investigate the elemental distribution of Mn_xO_y@PCNF. The mapping shows an even distribution of C, N, F, O, and Mn across the Mn_xO_y@PCNF surface (Figure 2a). TEM was used to analyze the structure of Mn_xO_y@PCNF further. Consistent with SEM and EDS analysis, TEM images of Mn_xO_y@PCNF (Figure 2b) clearly show porous structures in which spherical manganese oxide nanoparticles are homogeneously distributed on the porous carbon nanofiber matrix. Furthermore, manganese oxide nanoparticles are consistently small at about 13 nm (inset Figure 2c) without any significant agglomeration. The combination of well-dispersed and small particle sizes of manganese oxide nanoparticles corresponds to the improved accessible active site and thus enhances the electrochemical performance of the cathode.^[40]

Mechanical properties of Mn_xO_y@PCNF, CNF, and PCNF were also analyzed using a tensile test (Figure 2d). CNF shows the highest tensile modulus of elasticity (11.2 MPa) than PCNF (10.3 MPa) and Mn_xO_y@PCNF (9.4 MPa), indicating superior rigidity and

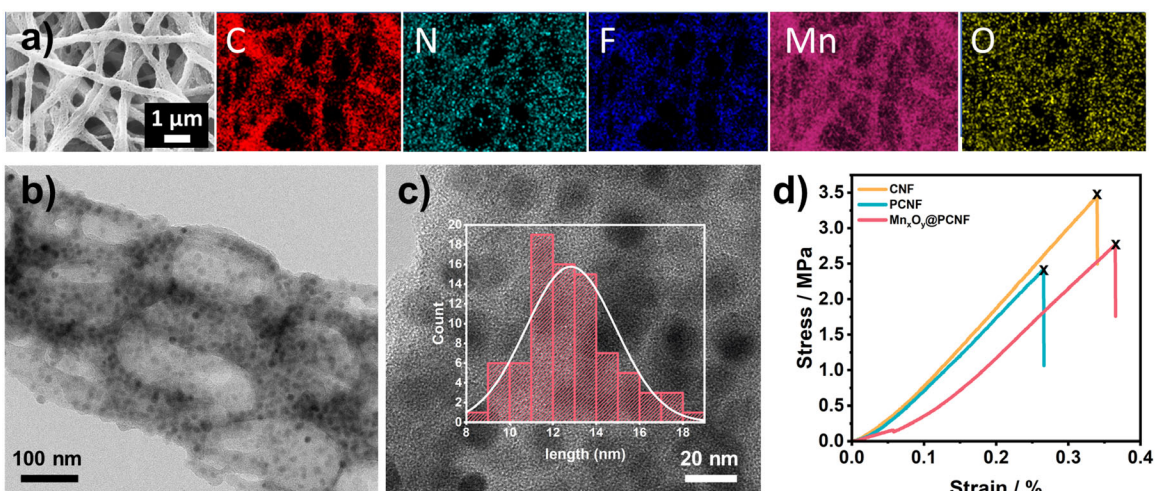


Figure 2. a) EDS mapping of Mn_xO_y@PCNF showing the distribution of C, N, F, Mn, and O elements. b–c) TEM images and corresponding particle size distribution of Mn_xO_y@PCNF. d) Tensile strength of CNF, PCNF, and Mn_xO_y@PCNF.

suitability as a robust support layer.^[41] Interestingly, despite having a lower modulus of elasticity, the layered $\text{Mn}_x\text{O}_y@\text{PCNF}$ exhibited a higher tensile strength (2.7 MPa) than PCNF (2.4 MPa). This can be attributed to the distinct 1D fibrous morphology of $\text{Mn}_x\text{O}_y@\text{PCNF}$, which facilitates more uniform stress distribution.^[42] In contrast, the globular fiber morphology of PCNF tends to induce localized stress concentrations, thereby reducing its tensile strength.^[43] Additionally, manganese oxide nanoparticles reinforce the matrix, enhancing the strength and toughness of $\text{Mn}_x\text{O}_y@\text{PCNF}$,^[44] making it suitable for applications requiring high surface area, mechanical robustness, and flexibility. This also highlights the effectiveness of sequential electrospinning in producing composite-derived carbon nanofibers with optimized properties.

The phase structure of CNF, PCNF, and $\text{Mn}_x\text{O}_y@\text{PCNF}$ was analyzed using X-ray diffraction (XRD). CNF and PCNF show similar XRD patterns (Figure 3a), in which the broad peak at $\approx 26^\circ$ belongs to (002) carbon plane,^[45] confirming the carbonization process of polymeric backbones. The (002) carbon peak still can be seen in $\text{Mn}_x\text{O}_y@\text{PCNF}$ with additional MnO_2 peaks (JCPDS card no. 04-007-3894) and Mn_3O_4 peaks (JCPDS card no. 04-007-9639).^[46,47] From thermogravimetric analysis (TGA) analysis (Figure S3, Supporting Information), manganese oxides in $\text{Mn}_x\text{O}_y@\text{PCNF}$ constitute around 36%.

X-ray photoelectron spectroscopy (XPS) is then used to analyze surface chemical bonding of $\text{Mn}_x\text{O}_y@\text{PCNF}$. Wide-XPS spectra show that $\text{Mn}_x\text{O}_y@\text{PCNF}$ comprises C, F, N, Mn, and O elements (Figure 3b). The existence of F and N peaks confirms the successful decomposition of PAN and PTFE into dual-doping F–N carbon during the carbonization process.^[26] The existence of F and N doping is also reconfirmed from C 1s spectra (Figure 3c) that consisted of CF_2 , CF, C–N, and C–C peaks at around 290.5, 288.3, 286.3, and 284.9 eV, respectively.^[48,49] Furthermore, $\text{Mn}_x\text{O}_y@\text{PCNF}$ possesses three N-doped carbon structures (Figure 3d), namely pyrrolic-N (400 eV), graphitic-N (401.3 eV), and pyridinic-N (398.7 eV).^[50] These N-doping potentially improve the zinc-ion transport by inducing negative charges of the carbon matrix.^[51,52]

High-resolution F 1s (Figure 3e) shows covalent and semi-ionic C–F peaks at 687.8 and 685.3 eV, respectively.^[48] $\text{Mn}_x\text{O}_y@\text{PCNF}$ has a high portion of semi-ionic C–F, which has been reported to improve the electrical conductivity of carbon.^[19] C–F bond can also improve surface wettability of the samples.^[13] Compared to single N-doped CNF, dual F–N doping samples (i.e., PCNF and $\text{Mn}_x\text{O}_y@\text{PCNF}$) have a significant drop in the contact angle, suggesting their better wettability (Figure 3h). The contact angles of PCNF (40°) and $\text{Mn}_x\text{O}_y@\text{PCNF}$ (35°) are less than half of CNF (101° , Figure 3h), signifying the advantageous wettability

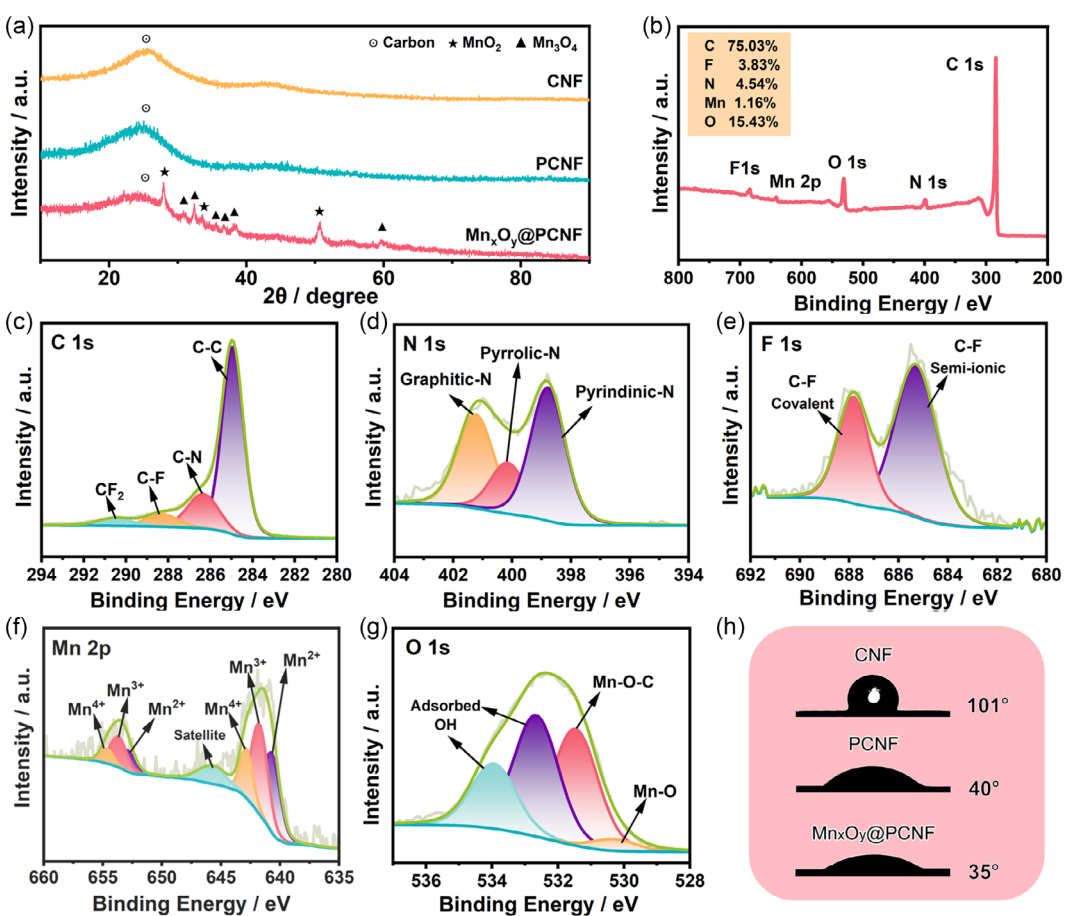


Figure 3. a) XRD of CNF, PCNF, and $\text{Mn}_x\text{O}_y@\text{PCNF}$. b) Wide-XPS spectra of $\text{Mn}_x\text{O}_y@\text{PCNF}$ and c–g) corresponding high-resolution spectra of C 1s, N 1s, F 1s, Mn 2p, and O 1s. h) Water contact angle of CNF, PCNF, and $\text{Mn}_x\text{O}_y@\text{PCNF}$ mat.

characteristics of the F-doped samples, promoting superior electrolyte penetration. The slightly lower contact angle of $\text{Mn}_x\text{O}_y@\text{PCNF}$ than PCNF is attributed to the presence of Mn_xO_y nanoparticles, which enhances its ionic affinity with Mn^{2+} ions in the electrolyte, thus improving its wettability.^[53] With enhanced surface wettability, $\text{Mn}_x\text{O}_y@\text{PCNF}$ optimizes electrolyte penetration across the cathode material, facilitating zinc-ion transport into active Mn_xO_y storage sites.^[39,54]

High-resolution Mn 2p (Figure 3f) is then deconvoluted into satellite (645.7 eV), Mn^{2+} (640.7/653 eV), Mn^{3+} (641.7/653.7 eV), and Mn^{4+} (642.8/654.6 eV),^[55,56] confirming the existence of MnO_2 and Mn_3O_4 phases. The O 1s spectra (Figure 3g) show $\text{Mn}-\text{O}-\text{C}$ (531.5 eV), $\text{Mn}-\text{O}$ (530.3 eV), and adsorbed OH (532.7 and 534 eV) peaks.^[57] $\text{Mn}-\text{O}-\text{C}$ peak signifies a strong interaction between carbon nanofiber and Mn_xO_y , facilitating rapid charge transfer.^[31] Based on density functional theory calculations, this interaction could weaken the electrostatic repulsion during intercalation and improve the kinetics of zinc ions.^[52]

Electrochemical tests were conducted by assembling the free-standing cathodes in coin cell configurations with zinc foil anodes and 0.3M MnSO_4 + 2.0M ZnSO_4 aqueous electrolyte. Cyclic voltammetry (CV) profiles of CNF, PCNF, and $\text{Mn}_x\text{O}_y@\text{PCNF}$ cathodes at 0.1 mV s⁻¹ (Figure 4a) show four distinct redox peaks. Peaks 1 and 2 in the oxidation region are associated with extracting Zn^{2+} and H^+ , while peaks 3 and 4 in the reduction region are the insertions of Zn^{2+} and H^+ .^[58] This $\text{Zn}^{2+}/\text{H}^+$ ion insertion-extraction storage mechanism is further supported by ex situ XRD measurement (Figure S6b, Supporting Information). Furthermore, among the three samples, $\text{Mn}_x\text{O}_y@\text{PCNF}$ shows the highest current peak with the largest area under the CV curve, indicating a high $\text{H}^+/\text{Zn}^{2+}$ ion storage ability.^[59]

Conventionally, the extraction-insertion of Zn^{2+} and H^+ in manganese-based cathodes is accompanied by the redox reaction of $\text{Mn}^{2+}/\text{Mn}^{3+}/\text{Mn}^{4+}$.^[60] In this case, the manganese-free cathodes (i.e., CNF and PCNF) exhibit similar redox peaks to those of $\text{Mn}_x\text{O}_y@\text{PCNF}$. This may occur due to the presence of Mn^{2+} ions

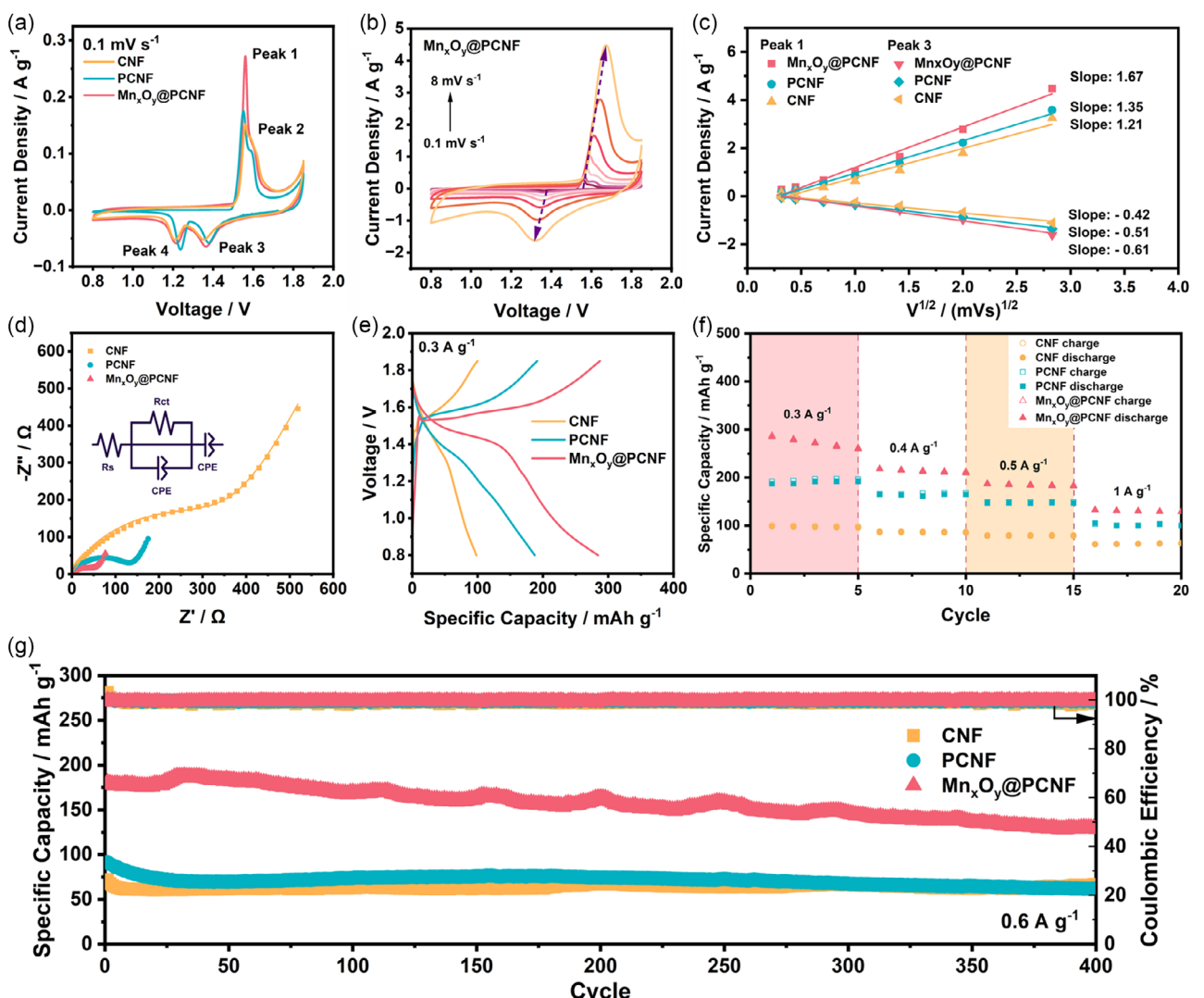


Figure 4. a) CV curve of CNF, PCNF, and $\text{Mn}_x\text{O}_y@\text{PCNF}$ at 0.1 mV s⁻¹. b) $\text{Mn}_x\text{O}_y@\text{PCNF}$'s CV curves at various scan rates. c) Plot of peak current versus square root of the scan rates with their respective linear fitting. d) EIS result of CNF, PCNF, and $\text{Mn}_x\text{O}_y@\text{PCNF}$. e) Voltage profile of CNF, PCNF, and $\text{Mn}_x\text{O}_y@\text{PCNF}$ at 0.3 A g⁻¹. f) Rate capability of CNF, PCNF, and $\text{Mn}_x\text{O}_y@\text{PCNF}$. g) Cycle curve of CNF, PCNF, and $\text{Mn}_x\text{O}_y@\text{PCNF}$ at 0.6 A g⁻¹.

in the electrolyte (i.e., MnSO_4) as one of the common salts to electrodeposit manganese oxides onto carbon electrodes via electrochemical techniques.^[61–63] Furthermore, the operating voltage window of zinc-ion batteries is favorable for the electrodeposition of manganese oxides.^[64] Therefore, manganese oxides can be electrodeposited onto CNF and PCNF during the battery activation step and thus exhibit redox peaks during CV scans. This is also proven by postmortem SEM-EDS images of CNF and PCNF (Figure S4, Supporting Information), which exhibit newly deposited manganese oxide layers after the electrochemical tests.

To further investigate the diffusion kinetics, multiscan rate CV tests were conducted on CNF, PCNF, and $\text{Mn}_x\text{O}_y@\text{PCNF}$ (Figure 4b and Figure S5, Supporting Information). Based on the Randles–Ševčík equation, the linear slope obtained from plotting the peak current against the square root of the scan rate can be used to evaluate the diffusion kinetics of the cathodes. A steeper linear slope indicates more efficient ion diffusion kinetics.^[65] Figure 4c shows that $\text{Mn}_x\text{O}_y@\text{PCNF}$ has the steepest slope, followed by PCNF and CNF. For dual F–N-doped samples, improved zinc-ion diffusion kinetics are related to the synergic effects of porous structure and increased surface wettability.^[17,66] This improves electrolyte infiltration into the cathodes, proven by the lower contact angle analysis (Figure 3h), ensuring efficient diffusion kinetics during charge and discharge.^[39] Furthermore, galvanostatic intermittent titration technique (GITT) measurements corroborate this result by determining the Zn ion diffusion coefficient ($D_{\text{Zn}^{2+}}$) of $\text{Mn}_x\text{O}_y@\text{PCNF}$ (Figure S7, Supporting Information). $\text{Mn}_x\text{O}_y@\text{PCNF}$ shows an average Zn ion diffusion coefficient of 8.5×10^{-10} and $1.7 \times 10^{-11} \text{ cm}^2 \text{ s}^{-1}$, during the discharge and charge step, respectively. This result is comparable to or even higher than previously reported studies, which span from 10^{-8} to 10^{-14} .^[67–71]

All of the results further support the idea that dual doping of the F–N and porous layer in $\text{Mn}_x\text{O}_y@\text{PCNF}$ can effectively boost Zn ion transport.

The effect of dual F–N doping and Mn_xO_y porous carbon nanofiber on charge transfer resistance is then analyzed using electrochemical impedance spectroscopy (EIS) measurements. The fitted Nyquist plots with an equivalent circuit are depicted in the inset of Figure 4d. Compared to a single N-doped sample (i.e., CNF), dual F–N doping samples of PCNF and $\text{Mn}_x\text{O}_y@\text{PCNF}$ show much lower charge transfer resistance (R_{ct}). $\text{Mn}_x\text{O}_y@\text{PCNF}$, PCNF, and CNF have the R_{ct} values of 52, 131, and 346 Ω , respectively. Low R_{ct} is associated with rapid kinetics, enabling the battery to store and release more charges efficiently.^[72] In line with XPS results, this can be attributed to the existence of graphitic-N and semi-ionic C–F, which enhances the conductivity of $\text{Mn}_x\text{O}_y@\text{PCNF}$.^[73] Furthermore, with the high electronegativity of F, the semi-ionic C–F bond facilitates electron delocalization in the carbon network, potentially enhancing zinc ions transport.^[54] Additionally, the lowest R_{ct} value of $\text{Mn}_x\text{O}_y@\text{PCNF}$ showcases its superior 1D structure, which facilitates superior charge conduction along the fiber direction, enabling faster charge transfer compared to the globular structure of PCNF.^[74]

To prove the advantages of dual F–N-doped carbon for manganese oxide-based cathode, the specific capacity of all samples was tested. Among all samples, $\text{Mn}_x\text{O}_y@\text{PCNF}$ yields high specific capacity of 284 mAh g^{-1} at 0.3 A g^{-1} (Figure 4e), much higher than CNF (100 mAh g^{-1}), PCNF (187 mAh g^{-1}), and some reported manganese oxide-based cathodes (Table S2, Supporting Information). This shows that a porous structure, along with improved wettability and conductivity, can lead to optimized specific capacity of manganese oxide-based cathodes. The porous

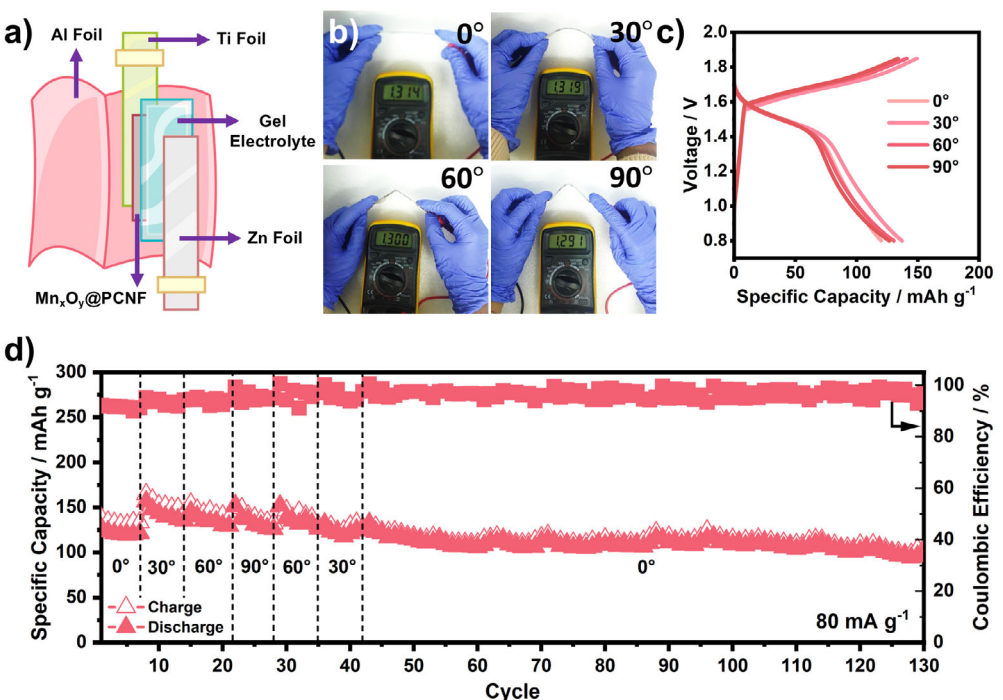


Figure 5. a) Schematic of flexible quasisolid pouch-cell zinc-ion battery with $\text{Mn}_x\text{O}_y@\text{PCNF}$. b) OCV values. c) CV profile of flexible battery at various bending angles. d) Cycling stability of flexible battery at different bending angles of 0° , 30° , 60° , and 90° at 80 mA g^{-1} .

structure enhances access to well-dispersed Mn_xO_y sites, while better wettability improves electrolyte–electrode contact, enhancing zinc-ion transport.^[14] These advantages and improved conductivity enhance charge transfer during charge and discharge, resulting in high specific capacity for $Mn_xO_y@PCNF$.^[19]

The rate capability of $Mn_xO_y@PCNF$ at various current densities is shown in Figure 4f. In all current densities, $Mn_xO_y@PCNF$ shows higher capacity than CNF and PCNF, showing average capacities of 271, 212, 184, and 130 mAh g⁻¹ at 0.3, 0.4, 0.5, and 1 A g⁻¹, respectively. The capacity of $Mn_xO_y@PCNF$ at 1 A g⁻¹ exceeds that of non-doped or single N-doped carbon/manganese oxide composite cathodes,^[75–77] which could be attributed to improved conductivity from dual F–N-doped carbon and rapid charge transfer induced by strong interaction between carbon nanofiber and Mn_xO_y via Mn–O–C bond.^[31] Cycling test at current density of 0.6 A g⁻¹ was then carried out to evaluate the stability of CNF, PCNF, and $Mn_xO_y@PCNF$ (Figure 4g). After 400 cycles, $Mn_xO_y@PCNF$ retains 70% of its initial capacity and delivers specific capacity of 177 mAh g⁻¹, much higher than that for CNF (65 mAh g⁻¹) and PCNF (62 mAh g⁻¹).

To evaluate the potential implementation of $Mn_xO_y@PCNF$ in flexible zinc-ion batteries, $Mn_xO_y@PCNF$ cathode was used in a pouch-cell configuration with PVA-based quasisolid electrolyte (Figure 5a). Flexible zinc-ion batteries with $Mn_xO_y@PCNF$ cathode can deliver relatively stable open circuit voltage (OCV, Figure 5b) of about 1.3 V and capacity of 130 mAh g⁻¹ under various bending angles of 0°–90° (Figure 5c), highlighting its robustness related to its dual layer structure. Furthermore, from the cycling stability test (Figure 5d), the flexible battery can achieve high stability by retaining 80% of its initial capacity after 130 cycles. The flexible $Mn_xO_y@PCNF$ battery also performs similarly to previously reported works, with improved stability across various bending conditions (Table S3, Supporting Information), approving its potential application in flexible electronics.

3. Conclusion

The layered structure design successfully yields a mechanically robust, self-supported, and porous cathode. It consists of manganese oxide nanoparticles embedded in porous F–N-doped carbon nanofibers, reinforced by CNF layer to enhance the mechanical strength, produced via sequential electrospinning. With porous architecture and high surface area, $Mn_xO_y@PCNF$ possesses more accessible Mn_xO_y storage sites. Dual F–N doping enhances the cathode surface's wettability for better electrolyte penetration, promoting efficient zinc-ion transport. It also improves conductivity, facilitating faster charge transfer. These benefits result in self-supported $Mn_xO_y@PCNF$ cathode with high specific capacity of 284 mAh g⁻¹ at 0.3 A g⁻¹. Furthermore, its favorable mechanical properties enable $Mn_xO_y@PCNF$ cathode for flexible pouch cells, achieving an average capacity of 130 mAh g⁻¹ across bending angles (0–90°) and retaining 80% capacity after 130 cycles. This work gives insight into developing high-performance self-supported cathodes to support the development of flexible zinc-ion batteries.

4. Experimental Section

Fabrication of $Mn_xO_y@PCNF$

PAN was used as a carbon–nitrogen source, while PTFE served as both a carbon–fluorine source and pore-forming agent. To fabricate $Mn_xO_y@PCNF$, solution-A was made by dissolving 1 g PAN (Mw 150,000, Sigma Aldrich) in 9 mL N,N-dimethylformamide. Separately, solution-B was prepared by dissolving 0.608 g PVA (Mw 85,000–124,000, Sigma Aldrich) in 7 mL deionized (DI) water at 80 °C (2 h). After that, 1.8 μL of 5 wt% boric acid solution (Merck), 2.3 mL PTFE dispersion (60 wt%, ITNANO), and 0.608 g $Mn(Ac)_2$ (Sigma Aldrich) were added sequentially to solution-B, before being stirred overnight. To fabricate $Mn_xO_y@PCNF$, solution-A was first electrospun at 9.6 kV with flow rate and humidity of 0.02 mL min⁻¹ and 45%, respectively. Subsequently, solution-B was electrospun above the obtained PAN layer at a flow rate of 0.008 mL min⁻¹ and 60% humidity. The resulting nanofiber mat was stabilized at 200 °C (3 h) to enhance thermal stability before being subjected to carbonization at 600 °C (2 h) under N_2 .^[29] During carbonization, PAN decomposed into nitrogen-doped carbon^[31,78] while PTFE yielded fluorine-doped carbon and porous structures,^[26] resulting in free-standing $Mn_xO_y@PCNF$. For comparison, samples with PAN layer only and a similar sample but without the addition of $Mn(Ac)_2$ were also fabricated and labeled as CNF and PCNF, respectively.

Material Characterizations

The sample's morphology was determined using SEM coupled with EDS (SEM-EDS Hitachi SU3500). Rigaku SmartLab was used to collect XRD spectra. XPS spectra were acquired via Kratos Axis Supra⁺. TEM images were obtained using Tecnai G2 20 S-Twin. TGA was conducted using Themys One. Surface area was analyzed using Micromeritics Tristar 3020. Tensile test of the samples was assessed using Instron 5985 with sample width, gauge length, and grip separation rate of 10, 20, and 0.2 mm min⁻¹, respectively. Ex situ XRD tests were carried out using Bruker D8 Advance at different conditions, i.e., discharge of 0.8 V and charge of 1.85 V at a current density of 0.3 A g⁻¹. The cells were disassembled, and the $Mn_xO_y@PCNF$ cathode was removed, washed with DI water, and dried before being transferred to the XRD instrument.

Battery Fabrication and Electrochemical Measurements

The free-standing cathodes (1×1 cm²) with a mass loading of 0.6 ± 0.1 mg cm⁻² were assembled with a glass fiber separator, Zn foil, and a 2.0M $ZnSO_4 + 0.3M MnSO_4$ aqueous electrolyte in CR2032 coin cells. Galvanostatic charge–discharge measurement was analyzed using the Neware battery tester. An initial activation step at 0.05 A g⁻¹ (5 cycles) was carried out, followed by cycling stability tests at 0.6 A g⁻¹. Rate capability was assessed at current densities of 0.3–1 A g⁻¹. CV was performed using a Corrtest CS150 at potential 0.8–1.85 V and a scan rate of 0.1–8 mV s⁻¹. Metrohm Autolab PGSTAT502N was used to measure EIS. The GITT test was conducted at a rate of 60 mA g⁻¹ with a 30-min pulse followed by a 60-min resting period. The diffusion coefficient of Zn^{2+} ion ($D_{Zn^{2+}}^{GITT}$) was then calculated according to the previous study.^[79] For the flexible battery, $Mn_xO_y@PCNF$ cathode (2×1 cm²) was assembled with a glass fiber separator, Zn foil, and gel electrolyte ($Zn(Ac)_2 + Mn(Ac)_2$) in a pouch-cell configuration. Galvanostatic charge–discharge tests were conducted under various bending angles (0°, 30°, 60°, and 90°) at 80 mA g⁻¹.

Acknowledgement

The authors acknowledge the funding from Institut Teknologi Bandung through the 2025 ITB research program.

Conflict of Interest

The authors declare no conflict of interest.

Data Availability Statement

The data that support the findings of this study are available from the corresponding author upon reasonable request.

Keywords: doping · electrospinning · manganese oxides · nanostructure · self-supported cathodes

- [1] Y. Li, B. Liu, J. Ding, X. Han, Y. Deng, T. Wu, K. Amine, W. Hu, C. Zhong, J. Lu, *Batteries Supercaps* 2021, 4, 60.
- [2] Q. Zheng, L. Liu, Z. Hu, Z. Tang, H. Lu, Y. Gao, J. Wang, Y. Song, C. Han, W. Li, *Adv. Funct. Mater.* 2025, 2504782.
- [3] J. S. Yeon, S. K. Park, S. Kim, S. V. Mohite, W. Il Kim, G. Jang, H.-S. Jang, J. Bae, S. M. Lee, W. G. Hong, B. H. Kim, Y. Kim, H. S. Park, *Carbon Energy* 2024, 6, e469.
- [4] B. Zhao, P. Jia, L. Yu, Y. Song, Z. Li, Y. Wang, R. Feng, H. Li, X. Cui, H. Cui, Y. Wang, M. Zhao, X. Zhao, X. Fang, Y. Pan, *J. Energy Storage* 2023, 73, 109174.
- [5] C. Xu, Y. Niu, V. Ka-Man Au, S. Gong, X. Liu, J. Wang, D. Wu, Z. Chen, *J. Energy Chem* 2024, 89, 110.
- [6] Y. Sun, Y. Liu, Z. Wang, X. Zhao, K. Cai, *Chem. Eng. J.* 2024, 484, 149573.
- [7] M. Gao, Z. Tang, M. Wu, J. Chen, Y. Xue, X. Guo, Y. Liu, Q. Kong, J. Zhang, *J. Alloys Compd* 2021, 857, 157554.
- [8] X. Li, C. Li, G. Guan, X. Zhang, J. Xiang, *Vacuum* 2024, 230, 113697.
- [9] Q. Zheng, Z. Hu, L. Liu, H. Lu, X. Wang, Y. Lei, C. Han, W. Li, *J. Mater. Chem. A* 2024, 12, 21531.
- [10] M. Boshir Ahmed, J. Alom, M. S. Hasan, M. Asaduzzaman, M. S. Rahman, R. Hossen, M. Abu Hasan Johir, M. Taufiq Alam, J. L. Zhou, Y. Zhu, M. Zargar, *ChemNanoMat* 2023, 9, e202200482.
- [11] L. Wang, J. Huang, X. Hu, Z. Huang, M. Gao, D. Yao, T. Taylor Isimjan, X. Yang, *J. Colloid Interface Sci.* 2024, 660, 989.
- [12] X. Shi, P. Sun, X. Wang, W. Xiang, Y. Wei, X. Lv, X. Sun, *J. Colloid Interface Sci.* 2025, 679, 1029.
- [13] J. Wu, X. Yang, J. Zhang, S. Guan, J. Han, J. Wang, K. Li, G. Zhang, T. Guan, *J. Power Sources* 2022, 548, 232065.
- [14] X. Wen, Y. Zhong, S. Chen, Z. Yang, P. Dong, Y. Wang, L. Zhang, Z. Wang, Y. Jiang, G. Zhou, J. Liu, J. Gao, *Adv. Sci.* 2024, 11, 2309555.
- [15] S. Liu, X. Yan, J. Cong, P.-Y. Li, S.-H. Luo, *J. Solid State Chem* 2024, 335, 124695.
- [16] Y. Ren, Q. Li, Q. Liu, W. Jiang, H. Qiu, Y. Zhang, W. He, *Diam Relat Mater* 2025, 151, 111730.
- [17] W. Na, J. Jun, J. W. Park, G. Lee, J. Jang, *J. Mater. Chem. A* 2017, 5, 17379.
- [18] J.-C. Wu, X.-C. Shen, H. Wang, D.-J. Deng, S.-Q. Wu, Y. Gong, L.-H. Zhu, L. Xu, H.-N. Li, *Mater. Today Phys.* 2023, 38, 101274.
- [19] S. G. Peera, R. S. Menon, S. K. Das, A. Alfantazi, K. Karuppasamy, C. Liu, A. K. Sahu, *Coord. Chem. Rev.* 2024, 500, 215491.
- [20] B. He, L. Feng, G. Hong, L. Yang, Q. Zhao, X. Yang, S. Yin, Y. Meng, D. Xiao, Y. Wang, J. Ai, *Chem. Eng. J.* 2024, 490, 151636.
- [21] S. Huang, Y. Li, Y. Feng, H. An, P. Long, C. Qin, W. Feng, *J. Mater. Chem. A* 2015, 3, 23095.
- [22] T. Zhou, B. Wu, C. Li, X. Zhang, W. Li, H. Pang, *ChemSusChem* 2024, 17, e202400890.
- [23] T. Zhang, J. Ju, Z. Zhang, D. Su, Y. Wang, W. Kang, *J. Energy Chem* 2024, 98, 562.
- [24] D. Zhang, C. Zhang, Z. Huo, J. Sun, G. Liu, X. Liu, C. Yu, *Materials Letters* 2024, 376, 137314.
- [25] S. Wu, Y. Zhu, F. Yi, Z. Cui, A. Huang, *J. Energy Storage* 2024, 103, 114358.
- [26] J. Yan, K. Dong, Y. Zhang, X. Wang, A. A. Aboalhassan, J. Yu, B. Ding, *Nat. Commun.* 2019, 10, 5584.
- [27] L. Chen, X. Lin, J. Gao, M. Zou, Y. Huang, G. Zhao, J. Li, *Electrochim. Acta* 2022, 403, 139654.
- [28] X. Cao, W. Chen, P. Zhao, Y. Yang, D.-G. Yu, *Polymers* 2022, 14, 3990.
- [29] E. Frank, L. M. Steudle, D. Ingildeev, J. M. Spörl, M. R. Buchmeiser, *Angew. Chem. Int. Ed.* 2014, 53, 5262.
- [30] H. Fong, I. Chun, D. H. Reneker, *Polymer* 1999, 40, 4585.
- [31] R. Akmalia, F. H. Hamid, F. D. Azura, Y. Irmawati, Q. Yan, A. Sumboja, *ACS Appl. Energy Mater.* 2024, 7, 7064.
- [32] O. Elishav, V. Beilin, O. Rozent, G. E. Shter, G. S. Grader, *J. Polym. Sci., Part B: Polym. Phys.* 2018, 56, 248.
- [33] E. Josef, R. Yan, R. Guterman, M. Oschatz, *ACS Appl. Energy Mater.* 2019, 2, 5724.
- [34] B. Ari, E. Inger, A. K. Sunol, N. Sahiner, *J. Compos. Sci.* 2024, 8, 338.
- [35] H. Liu, Y. Liu, H. Da, R. Yuan, *RSC Adv.* 2018, 8, 13964.
- [36] D. Seo, M.-R. Kim, J. Kyu Song, E. Kim, J. Koo, K.-C. Kim, H. Han, Y. Lee, C. Won Ahn, *ChemElectroChem* 2022, 9, e202101344.
- [37] L. Zhang, G. Xia, Z. Guo, D. Sun, X. Li, X. Yu, *J. Power Sources* 2016, 324, 294.
- [38] M. Chen, S. Xie, X. Zhao, L. Peng, Y. Li, J. Zhang, M. Han, X. Liang, Q. Liu, Y. Zhang, Z. Chen, Q. Chen, *ACS Sustain. Chem. Eng.* 2022, 10, 12188.
- [39] A. Lata, A. Kumar, G. Biswas, N. Chanda, R. K. Arun, *Energy Adv.* 2023, 2, 797.
- [40] C. Bischoff, O. Fitz, C. Schiller, H. Gentischer, D. Biro, H.-M. Henning, *Batteries* 2018, 4, 44.
- [41] J. V. Sanchaniya, I. Lasenko, V. Vijayan, H. Smogor, V. Gobins, A. Kobeissi, D. Goljandini, *Polymers* 2024, 16, 992.
- [42] J. Yao, C. W. M. Bastiaansen, T. Peijs, *Fibers* 2014, 2, 158.
- [43] T. U. Rashid, R. E. Gorga, W. E. Krause, *Adv. Eng. Mater.* 2021, 23, 2100153.
- [44] N. Zhang, R. Zhao, D. He, Y. Ma, J. Qiu, C. Jin, C. Wang, *J. Alloys Compd* 2019, 784, 244.
- [45] Y. Irmawati, D. A. Tan, F. Balqis, F. Iskandar, A. Sumboja, *Nanoscale* 2024, 16, 1833.
- [46] S. K. Chondath, A. P. K. Sreekala, C. Farzeena, S. N. Varanakkottu, M. M. Menamparambath, *Nanoscale* 2022, 14, 11197.
- [47] H. Eraky, J. J. Dynes, A. P. Hitchcock, *J. Electron Spectros. Relat. Phenomena* 2024, 274, 147452.
- [48] F. Liu, Z. Li, Y. Li, Y. Feng, W. Feng, *Carbon* 2021, 181, 9.
- [49] L. Yang, B. He, M. Li, S. Li, D. Xiao, Y. Wang, Y. Meng, Q. Zhao, Q. Yue, W. Feng, *Inorg. Chem. Front.* 2024, 11, 4672.
- [50] J. Wu, C. Cheng, S. Lu, B. Zhang, Y. Shi, *Trans. Tianjin Univ.* 2024, 30, 369.
- [51] F. H. Hamid, J. Karunawan, Y. Irmawati, B. T. Laksono, E. Peiner, H. S. Wasisto, F. Iskandar, A. Sumboja, *Electrochim. Acta* 2023, 471, 143384.
- [52] X. Li, Q. Zhou, Z. Yang, X. Zhou, D. Qiu, H. Qiu, X. Huang, Y. Yu, *Energy Environ. Mater.* 2023, 6, e12378.
- [53] C.-C. Kan, M. C. Aganon, C. M. Futalan, M. L. P. Dalida, *J. Environ. Sci.* 2013, 25, 1483.
- [54] H. An, Y. Li, P. Long, Y. Gao, C. Qin, C. Cao, Y. Feng, W. Feng, *J. Power Sources* 2016, 312, 146.
- [55] F. Zeng, Y. Pan, Y. Yang, Q. Li, G. Li, Z. Hou, G. Gu, *Electrochim. Acta* 2016, 196, 587.
- [56] J. X. Flores-Lasluisa, M. García-Rodríguez, D. Cazorla-Amorós, E. Morallón, *Carbon* 2024, 225, 119147.
- [57] D. Zhang, C. Zhang, X. Zheng, Y. Zhao, X. Shi, B. Luo, Y. Li, G. Liu, X. Liu, C. Yu, *Int. J. Miner. Metall. Mater.* 2023, 30, 1152.
- [58] Y. Zhang, X. Lin, X. Tang, K. Hu, X. Lin, G. Xie, X. Liu, H.-J. Qiu, *ACS Appl. Nano Mater.* 2022, 5, 12729.
- [59] Y. Huang, Y. Peng, Q. Ouyang, Q. Feng, H. Wang, D. Zheng, F. Wang, X. Lu, Q. Liu, *Energy Storage Mater.* 2024, 70, 103476.
- [60] B. Zhang, P. Dong, S. Yuan, Y. Zhang, Y. Zhang, Y. Wang, *Chem Bio Eng.* 2024, 1, 113.
- [61] M. C. Nascimento, E. C. Silva, J. C. M. Costa, B. L. Pereira, R. R. Passos, L. A. Pocrifka, *J. Solid State Electrochem.* 2020, 24, 2543.
- [62] A. Raveendran, M. Chandran, M. R. Siddiqui, S. M. Wabaidur, M. Eswaran, R. Dhanusuraman, *J. Mater. Sci.: Mater. Electron.* 2023, 34, 2018.
- [63] C. Qin, J. Luo, D. Zhang, L. Brennan, S. Tian, A. Berry, B. M. Campbell, B. Sadler, *ACS Nanosci. Au* 2023, 3, 310.
- [64] R. Liang, J. Fu, Y.-P. Deng, Y. Pei, M. Zhang, A. Yu, Z. Chen, *Energy Storage Mater.* 2021, 36, 478.
- [65] T. Shao, Y. Zhang, T. Cao, Y. Yang, Z. Li, H. Liu, Y. Wang, Y. Xia, *Chem. Eng. J.* 2022, 431, 133735.
- [66] Y. Shao, Y. Cui, C. Wang, Q. Yang, S. Hong, Y. Tang, Y. Zhang, X. Guo, L. Zhang, L. Song, J. Qiu, *Small* 2023, 19, 2300107.
- [67] N. H. Hawari, A. Prayogi, Y. Irmawati, P. B. Persada, T. A. Ivandini, A. Zulfia, H. Judawisastra, Q. Yan, A. Sumboja, *J. Energy Storage* 2024, 100, 113715.
- [68] C. Wang, H. Liu, L. Han, J. Zhang, R. Liu, F. Kong, *Mater. Res. Bull.* 2025, 191, 113543.
- [69] W. Li, W. Li, L. Qin, Z. Xu, L. Liu, G. Fang, S. Chen, *J. Energy Storage* 2025, 122, 116692.
- [70] X. Pang, Q. Liu, M. Li, Z. Fan, C. Yang, J. Qiu, M. He, L. Zang, *J. Alloys Compd* 2025, 1031, 181006.
- [71] K. Wang, L. Wang, G. Li, S. Chen, L. Chen, S. Wang, P. An, J. Li, S. Zhang, *Colloids Surf. A: Physicochem. Eng. Asp.* 2025, 719, 137046.
- [72] L. Hong, X. Wu, C. Ma, W. Huang, Y. Zhou, K.-X. Wang, J.-S. Chen, *J. Mater. Chem. A* 2021, 9, 16814.

- [73] D. Hulicova-Jurcakova, M. Seredych, G. Q. Lu, T. J. Bandosz, *Adv. Funct. Mater.* **2009**, *19*, 438.
- [74] W. Song, R. Shi, L. Zhang, T. Gao, W. Lian, K. Liu, X. Niu, Y. Wu, K. Nie, *Dalton Trans.* **2022**, *51*, 10221.
- [75] J. Li, X. Yang, D. Ma, J. Liu, C. Ma, N. Liu, L. Lu, T. Wang, X. Pang, Y. Yang, Q. Zhang, X. Li, *J. Colloid Interface Sci.* **2024**, *676*, 927.
- [76] L. Chen, Z. Yang, H. Qin, X. Zeng, J. Meng, *J. Power Sources* **2019**, *425*, 162.
- [77] J. Pu, Y. Xue, Z. Ji, J. Cao, X. Shen, H. Zhou, A. Yuan, L. Kong, *J. Colloid Interface Sci.* **2025**, *686*, 27.
- [78] F. Haidar Hamid, Y. Irmawati, A. Nur Estri, A. Hadziq Haidar, A. Sumboja, *Batteries Supercaps* **2025**, e202500021.
- [79] N. Ding, J. Xu, Y. X. Yao, G. Wegner, X. Fang, C. H. Chen, I. Lieberwirth, *Solid State Ion.* **2009**, *180*, 222.

Manuscript received: March 27, 2025

Revised manuscript received: May 31, 2025

Version of record online:
